

# Assessing Uncertainties in the Predicted Very-High-Energy Flux of Globular Clusters in the Cherenkov Telescope Array Era

Hambeleleni Ndiyavala-Davids<sup>1,2\*</sup>, Christo Venter<sup>1</sup>, Andreas Kopp<sup>1</sup>,  
and Michael Backes<sup>3,1</sup>

<sup>1</sup>Centre for Space Research, North-West University, Potchefstroom Campus, Private Bag X6001, Potchefstroom 2520, South Africa

<sup>2</sup>University of Namibia, Department of Science Foundation, Khomasdal Campus, Private Bag 13301, Windhoek, Namibia

<sup>3</sup>University of Namibia, Department of Physics, Windhoek Campus, Private Bag 13301, Windhoek, Namibia

Accepted 2020 November 13. Received 2020 November 7; in original form 2020 October 19

## ABSTRACT

Terzan 5 is the only Galactic globular cluster that has plausibly been detected in the very-high-energy range. Stacking upper limits by H.E.S.S. on the integral  $\gamma$ -ray flux of a population of other globular clusters are very constraining for leptonic cluster emission models. We demonstrate that uncertainty in model parameters leads to a large spread in the predicted flux, and there are indeed regions in parameter space for which the stringent stacking upper limits are satisfied. We conduct two more case studies: we study the uncertainties in differential TeV flux for M15, showing that our model can satisfy the stringent MAGIC upper limits for this cluster, for typical cluster parameters. We also calculate the differential flux at TeV energies for  $\omega$  Cen, from which five pulsars have recently been detected at radio energies. It is thus important to increase measurement accuracy on key model parameters in order to improve predictions of cluster fluxes so as to better guide the observational strategy of the Cherenkov Telescope Array.

**Key words:** Globular cluster: general - pulsars: general - gamma rays: stars - radiation mechanisms: non-thermal

## 1 INTRODUCTION

Ndiyavala et al. (2018) predict that tens of Galactic globular clusters (GCs) may be detectable within a reasonable amount of observation time for the next-generation Cherenkov Telescope Array (CTA). However, emission models predict quite a wide range of fluxes depending on how well constrained the model parameters are. There are a number of leptonic and hadronic models that predict the radiated spectrum by GCs. For example, Harding et al. (2005); Venter & de Jager (2005); Zajczyk et al. (2013) considered the cumulative pulsed curvature radiation (CR) spectrum from an ensemble of millisecond pulsars (MSPs) embedded in a GC due to leptons being accelerated within the pulsar magnetospheres. Furthermore, Bednarek & Sitarek (2007); Venter & de Jager (2008); Venter et al. (2009); Venter & de Jager (2010); Cheng et al. (2010); Kopp et al. (2013); Zajczyk et al. (2013) all assume a leptonic origin of the unpulsed GC emission where pulsars inject accelerated leptons that radiate synchrotron radiation (SR) and inverse Compton (IC) emission as they traverse the GC. Ndiyavala et al.

(2019) fit multi-wavelength data of Terzan 5 with a leptonic model that invokes unpulsed SR and IC components to model the radio and TeV data and cumulative pulsed CR to fit the *Fermi* Large Area Telescope (LAT) data. The authors also explain the hard *Chandra* X-ray spectrum via a “new” cumulative pulsed SR component from electron-positron pairs within the pulsar magnetospheres. Other models assume astrophysical objects such as white dwarfs that inject relativistic leptons into the GC (Bednarek 2012) or a  $\gamma$ -ray burst remnant that accelerates hadronic particles and secondary leptons, which contribute to the high-energy emission from GCs (Domainko 2011). Recently, Brown et al. (2018) concluded that a combination of cumulative CR emission from MSPs and dark matter annihilation may explain the GeV emission detected by *Fermi*-LAT from 47 Tucanae.

The theoretical expectations above are motivated by broadband detections of GCs. The *Fermi*-LAT has detected about 20  $\gamma$ -ray sources associated with GCs in the GeV band (Abdo et al. 2009; Kong et al. 2010; Tam et al. 2011; Zhang et al. 2016). In this paper, we focus on the very-high-energy (VHE;  $E > 100$  GeV) band. The ground-based High Energy Stereoscopic System (H.E.S.S.) Cherenkov telescope, operating in a pointing mode at energies above

\* E-mail: hndiyavala@unam.na

100 GeV, has only plausibly<sup>1</sup> detected a single GC in our Galaxy, i.e., Terzan 5 (Abramowski et al. 2011). H.E.S.S. searched for VHE  $\gamma$ -ray emission from 15 other Galactic GCs and did not detect any of those; neither did they detect any significant signal using a stacking analysis (involving a live-time-weighted GC flux; Abramowski et al. 2013). Therefore, they derived integral flux upper limits from their single-GC and stacking analyses. Interpreting these upper limits, they noted that a simple scaling of existing theoretical predictions invoking IC from relativistic leptons produces a VHE flux that violates these limits<sup>2</sup>. Observations by other Cherenkov telescopes could only produce upper limits (e.g., Anderhub et al. 2009; McCutcheon 2009). Observations of the GC 47 Tucanae (NGC 104) were performed with H.E.S.S. leading to an upper limit on the integral  $\gamma$ -ray flux of  $F(E > 800 \text{ GeV}) < 6.7 \times 10^{-13} \text{ cm}^{-2}\text{s}^{-1}$  (Aharonian et al. 2009). Observations of the GC M15 by the Major Atmospheric Gamma Imaging Cherenkov Telescopes (MAGIC) provided a deep upper limit on  $F(E > 300 \text{ GeV})$ , i.e.,  $< 0.26\%$  of the Crab Nebula flux. Also, stringent differential flux upper limits were obtained on this source (Acciari et al. 2019). Although we focus on  $\gamma$ -rays, we note that GCs are broadband emitters, i.e., they are also detected in X-rays, optical, and radio and these data are typically modeled using an SR spectrum (Eger et al. 2010; Abdo et al. 2010; Clapson et al. 2011).

The aim of this paper is to assess uncertainties in the predicted VHE  $\gamma$ -ray flux of GCs for a given leptonic model and to give theoretical guidance to CTA's observational strategy. That is, we model the IC  $\gamma$ -ray flux expected from several GCs to see whether the predicted flux exceeds the CTA sensitivity and whether we can satisfy the H.E.S.S. upper limits with a range of predicted fluxes (due to parameter uncertainties). We argue that one cannot simply scale the model output among different GCs, since the range of predicted fluxes depends crucially (and non-linearly in some cases) on the unique input parameters plus their uncertainties per source. The use of a population of clusters versus a single cluster should furthermore reduce the uncertainty in the predicted stacked flux, which can be used to make a better informed decision of whether a particular model should indeed be discarded in light of measurements or not; conversely, such an approach may yield more stringent constraints on the model parameters, if a given model remains viable. We will specifically (1) model a population of GCs and compare the predicted *integral* fluxes with H.E.S.S. upper limits, (2) model both the Northern-hemisphere cluster, M15, and Southern-hemisphere one, Omega Cen ( $\omega$  Cen), and compare our results with *differential* flux upper limits. We chose these two GCs given the deep MAGIC

<sup>1</sup> The best-fit position of the source detected by H.E.S.S. is displaced from Terzan 5's position, but still falls within the tidal radius of the GC. The morphology of the detected VHE emission is asymmetric and extends beyond the tidal radius of the GC, also being larger than the H.E.S.S. point spread function; however, the estimated probability of a chance coincidence of Terzan 5 and an unrelated VHE source is below  $\sim 10^{-4}$ .

<sup>2</sup> Indeed, the TeV flux is most sensitive to the particle source strength, i.e., the combination of number of MSPs, acceleration efficiency, and average MSP spin-down power, but not exclusively so. Thus, observational upper limits would first and foremost constrain the source strength, but may also be used to constrain degenerate parameters such as the diffusion coefficient or target photon fields (e.g., average stellar temperature), if the source strength is fixed to some reasonable value. If, however, limits are stringent enough that the resulting model parameters are not deemed reasonable anymore (e.g., too low number of MSPs or spin-down values given independent measurements from other wavebands), one would have to discard or extensively revise the model under consideration.

upper limits found for M15, and given the recent radio pulsar detections in the case of the latter. We will illustrate that there are indeed regions in parameter space for which the stringent stacking upper limits by H.E.S.S. are satisfied, for some subset of free parameters, given their uncertainty. Yet larger parameter uncertainties and more free model parameters will only increase the uncertainty on the predicted flux, making it even easier to satisfy these observational constraints.

The rest of the paper is structured as follows. In Section 2, we briefly discuss the model and its free parameters. In Section 3, we discuss the method employed to calculate the IC flux expected from the GCs plus its errors derived using a Monte Carlo process. Section 4 describes the results. In Section 5 we offer our conclusion.

## 2 THE MODEL AND ITS FREE PARAMETERS

A large number of spectral components is expected from GCs (Ndiyavala et al. 2019). The unpulsed emission should transpire through the continuous injection of relativistic leptons by the MSPs into the ambient GC region (Bednarek & Sitarek 2007), which in turn produce unpulsed SR and IC emission when they encounter the cluster magnetic field as well as background (stellar and cosmic microwave background) photon components. We also expect cumulative pulsed SR and CR components initiated by primaries and electron-positron pairs from within the magnetospheres of MSPs embedded in the cluster (Harding et al. 2005; Venter & de Jager 2005; Zajczyk et al. 2013). In this paper, we focus on the VHE component. The model by Kopp et al. (2013) that we use here calculates the particle transport (including diffusion and radiation losses) in a spherically symmetric, stationary approach and predicts the spectral energy distribution (SED) from GCs for a very broad energy range by considering unpulsed SR and IC. The main free parameters of this model are (cf. Ndiyavala et al. 2018; Ndiyavala et al. 2019): cluster magnetic field ( $B$ ), power-law index ( $\Gamma$ ) of the injected particle spectrum (the particles are assumed to have undergone acceleration in inter-pulsar shocks; Bednarek & Sitarek 2007), number of GC stars ( $N_*$ ), distance to the cluster ( $d$ ), the average spin-down luminosity per pulsar ( $\langle \dot{E} \rangle$ ), the conversion efficiency of spin-down luminosity into particle acceleration ( $\eta$ ), and number of MSPs in the GC ( $N_{\text{MSP}}$ ). The latter three are linked to the normalization of the injection spectrum  $Q_0$  in the following way:

$$Q_0 = \begin{cases} \frac{L_{\text{eff}}}{\ln(E_{e,\text{max}}/E_{e,\text{min}})} & \text{if } \Gamma = 2.0, \\ \frac{L_{\text{eff}}(2-\Gamma)}{E_{e,\text{max}}^{2-\Gamma} - E_{e,\text{min}}^{2-\Gamma}} & \text{if } \Gamma \neq 2.0. \end{cases} \quad (1)$$

where

$$L_{\text{eff}} = \eta \langle \dot{E} \rangle N_{\text{MSP}} \quad (2)$$

is the effective luminosity, and  $E_{e,\text{min}}$  and  $E_{e,\text{max}}$  are the minimum and maximum particle energies, respectively. The model yields the differential VHE flux  $dN_\gamma/dE$ . One can obtain the integral flux via

$$F(E_\gamma \geq E_{\text{th}}) = \int_{E_{\text{th}}}^{E_{\gamma,\text{max}}} E_\gamma \frac{dN_\gamma}{dE} dE_\gamma \quad (3)$$

where  $E_{\text{th}}$  is the threshold energy for each cluster. We kept the spatial diffusion coefficient ( $\kappa$ ), the core radius ( $r_c$ ), the half-mass radius ( $r_h$ ), and the tidal radius ( $r_t$ ) as fixed parameters.

One should note that the free parameters of the model may be degenerate in the sense that changing several different parameters

can independently produce higher TeV flux predictions. Moreover, while we treat them as independent parameters, some might actually be correlated, e.g., the cluster magnetic field may scale with the number of embedded pulsars in the cluster (see, [Bednarek & Sitarek 2007](#)). Since we do not know the exact nature of such a correlation, for simplicity we treat the mentioned free parameters as being independent. One may consider the effect of assuming some correlations between parameters, thereby decreasing the number of free parameters, in future.

### 3 MONTE CARLO METHOD

#### 3.1 Integral Flux Upper Limits: the H.E.S.S. GC Population

[Venter & Kopp \(2015\)](#) applied a leptonic GC model to the population of clusters mentioned in [Abramowski et al. \(2013\)](#) to predict the live-time-averaged (stacked) flux and compare it to the H.E.S.S. stacking upper limits. They used fixed (best-guess) model parameters as noted in their Table 1, and used the inferred values from [Abdo et al. \(2010\)](#) for  $N_{\text{MSP}}$  where possible, and  $N_*$  values from [Lang \(1993\)](#), and obtained distances  $d$  and structural parameters<sup>3</sup>  $r_c$ ,  $r_{\text{hm}}$ , and  $r_t$  from [Harris \(1996\)](#). Typical values of  $\eta \sim 0.01$  ([Venter & de Jager 2005](#)),  $N_{\text{MSP}} \sim 25$ , and  $\langle \dot{E} \rangle \sim 2 \times 10^{34} \text{ erg s}^{-1}$  led to typical values of  $Q_0 \sim 10^{33-34} \text{ erg}^{-1} \text{ s}^{-1}$  for the source strength (see Equations [1] and [2]). They also used  $B = 5 \mu\text{G}$  and  $\Gamma = 2.0$  throughout, and assumed optical photons from the stellar population embedded in the GC plus cosmic microwave background (CMB) photons as target fields for their IC calculation (assuming an average stellar temperature of  $\langle T \rangle = 4500 \text{ K}$ ). They found that none of the predicted single-cluster spectra violated the H.E.S.S. TeV upper limits for individual sources. Their averaged flux furthermore satisfied the stringent stacking upper limits. However, they noted that different choices of parameters led to average fluxes that in some cases may exceed these limits. That is why we refine their calculation in this paper, now also including an estimation of uncertainties on the predicted VHE fluxes.

In this Section, we describe the method we employ for modelling the IC  $\gamma$ -ray flux expected from the 15 Galactic GCs observed by H.E.S.S. We follow the method of [Venter & de Jager \(2008\)](#) where they used a Monte Carlo technique to model the pulsed CR  $\gamma$ -ray flux and associated uncertainties expected from 100 MSPs hosted by a GC. Their calculated CR flux was randomised over the magnetic inclination ( $\alpha$ ) and observer ( $\zeta$ ) angles that are usually estimated from radio polarisation measurements involving the rotating vector model ([Manchester & Johnston 1995](#)), as well as taking into account the fixed, pulsar-specific parameters such as period  $P$  and period derivative  $\dot{P}$  (or  $\dot{E}$ ) of each MSP member. In our case, we use the same method to calculate the single-GC and stacked integral VHE flux of 15 GCs ([Abramowski et al. 2013](#)), with uncertainties due to the uncertainty in model parameters. We do this by randomising over seven free parameters as mentioned in Section 2:  $B$ ,  $\Gamma$ ,  $N_*$ ,  $d$ ,  $\eta$ ,  $\dot{E}$ , and  $N_{\text{MSP}}$ , in addition to fixing the structural and diffusion coefficient parameters as noted above.

We first apply the model of [Kopp et al. \(2013\)](#) to the population of clusters to obtain the differential spectrum (Section 2) for different parameter combinations, initially setting  $Q_0 = 1$  and only using four free parameters ( $B$ ,  $\Gamma$ ,  $N_*$ , and  $d$ ). We then calculate the integral flux using Equation (3) and obtain a spread of fluxes, based on the range of values we picked for these four parameters.

To indicate the build-up of a smooth flux distribution, we use the four free parameters for illustration (for the full modeling, we use seven). Figure 1 thus indicates how a distribution of  $\log_{10}$  of the integral flux becomes smooth as we increase the resolution at which each of four free parameters is sampled. A finer grid thus lead to a smoother distribution of fluxes.

Second, we indicate convergence of the flux distribution with an increase of the number of trials, again for four free model parameters. That is, we calculate the integral flux for  $N_t$  trials (each trial corresponding to a different parameter combination on a pre-defined grid), obtaining convergence as  $N_t$  gets close to or exceeds the number of unique combinations ( $N_{\text{comb}}$ ) of the four free parameters. Thus, we reproduce the last panel of Figure 1 to indicate convergence in Figure 2. We note that undersampling will not give a smooth flux distribution, but oversampling will lead to convergence.

We thirdly check for the convergence of the source strength parameter  $Q_0$  (see Figure 3) via two methods, using 47 Tucanae as an example. For the first method, we pick values of four relevant (different) parameters on a specified grid:  $\eta \in [0.005, 0.08]$  in steps of 0.005,  $\log_{10}(\dot{E}) \in [33.7, 34.7]$  in steps of 0.05,  $N_{\text{MSP}} \in [5, 150]$  in steps of 1, and  $\Gamma \in [1.7, 2.9]$  in steps of 0.1. For the second method, we randomise over the same four parameters  $\eta$ ,  $\log \dot{E}$ ,  $N_{\text{MSP}}$ , and  $\Gamma$ , for fixed  $E_{e,\text{min}} = 0.1 \text{ TeV}$  and  $E_{e,\text{max}} = 100 \text{ TeV}$ , within the parameter ranges given above (but not on a fixed grid). We conduct  $N_t = 10^6$  trials in both cases. The two different approaches yield very similar results, which also correspond to the values found by [Kopp et al. \(2013\)](#) as well as to the calculation by [Venter & Kopp \(2015\)](#), with the two peaks in the histogram only slightly shifted with respect to each other. Thus, sampling on a grid vs. randomly picking parameter values does not make too much of a difference in terms of the distribution of  $Q_0$ .

We lastly perform nested loops over the seven free model parameters to calculate  $Q_0(\Gamma, \eta, \langle \dot{E} \rangle, N_{\text{MSP}}) \neq 1$ , and multiply the correct flux, pre-calculated for  $Q_0 = 1$  and depending only on  $B$ ,  $\Gamma$ ,  $d$ , and  $N_*$ , by the actual value of  $Q_0$  to obtain the final differential and integral fluxes in observational units (see Equation [1] and the final panel of Figure 4 for the case of 47 Tucanae). The spread in flux reflects the uncertainty in model parameters. We use the observational threshold energy  $E_{\text{th}}$  associated with a particular cluster to calculate  $F(> E_{\text{th}})$ . In Figure 4, we randomly sample integral fluxes for a different total number of trials  $N_t$  from the grid of pre-calculated fluxes to show convergence as  $N_t \rightarrow N_{\text{comb}}$ .

#### 3.2 Differential Flux Predictions: M15 and $\omega$ Cen

MAGIC has recently published differential flux upper limits for M15 ([Acciari et al. 2019](#); see Section 4.2 for details on the source and VHE data). We applied the model of [Kopp et al. \(2013\)](#) to M15 to obtain the *differential* fluxes for each combination of seven free model parameters (see Section 2). Next, we calculated the final differential flux as described in Section 3.1.

We again use the method of [Venter & de Jager \(2008\)](#) to estimate the uncertainty in the differential flux of M15 at 13 different observer-defined energy bins ([Acciari et al. 2019](#)). Specifically, we logarithmically interpolate model fluxes to obtain predictions at the specified observational energies associated with the upper limits. Our parameter grid for M15 was chosen as follows:  $B \in [1, 3, 5, 7, 9] \mu\text{G}$ , injection spectral index  $\Gamma \in [1.7, 2.0, 2.3, 2.6, 2.9]$ ,  $N_* \in [2.05, 2.90, 4.10, 5.80, 8.20] \times 10^5$ ,  $d \in [5.20, 7.35, 10.4, 14.7, 20.8] \text{ kpc}$ ,  $\eta \in [0.003, 0.063]$  with steps of 0.005,  $\log_{10}(\dot{E}) \in [33.7, 34.7]$  with steps of 0.05, and the

<sup>3</sup> <http://gclusters.altervista.org/index.php>

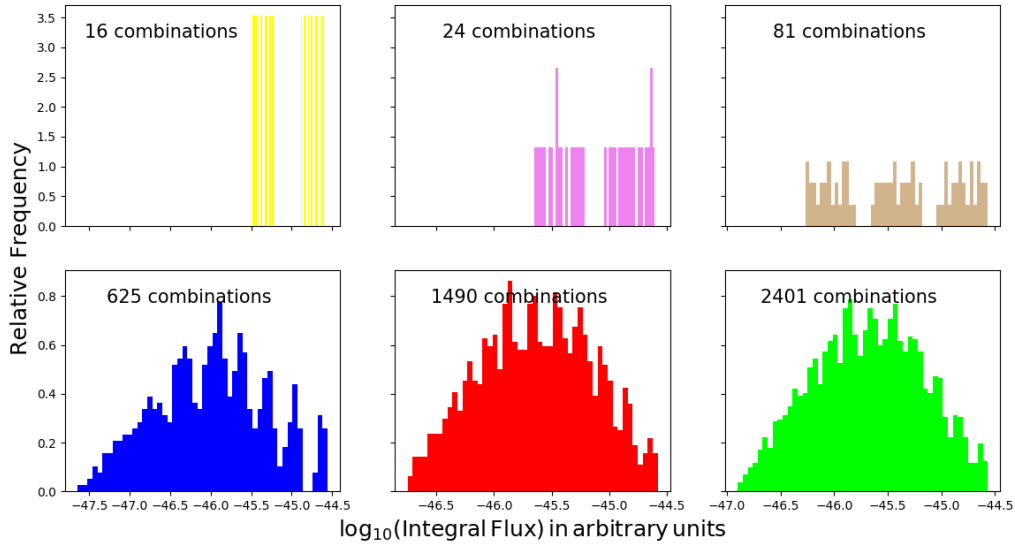


**Figure 1.** Histograms of  $\log_{10}(F(E > 0.72 \text{ TeV}))$  in arbitrary units, indicating how we build up statistics for the flux distribution for a finer grid in parameter space. The  $x$ -axis shows the integral fluxes while the  $y$ -axis shows the normalised frequency. The label indicates the number of unique parameter combinations in each case.

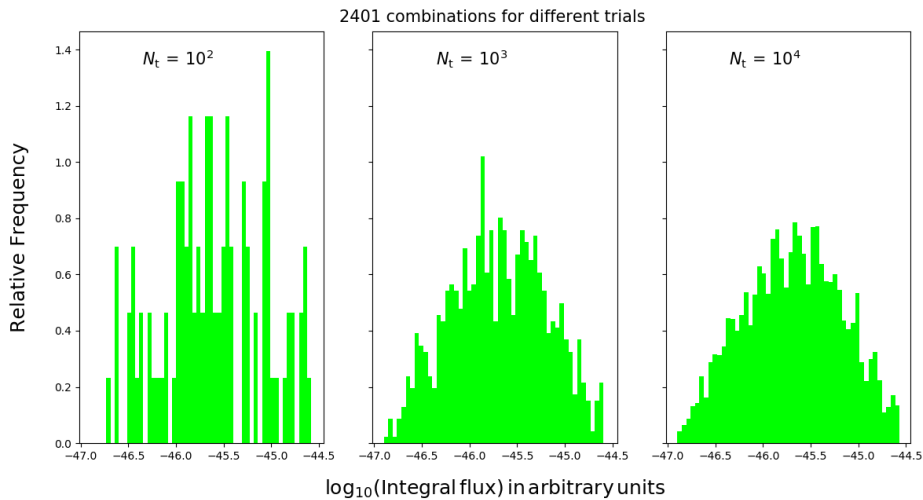


**Figure 2.** Histograms of  $\log_{10}(F(E > 0.72 \text{ TeV}))$

in arbitrary units, indicating convergence for  $N_t$  getting close to number of combinations ( $N_{\text{comb}}$ ) and  $N_t > N_{\text{comb}}$ .

number of MSPs  $N_{\text{MSP}} \in [8, 24]$ , in steps of 1. In the case of  $\omega \text{ Cen}$ , we used the same  $B$  and  $\Gamma$  range as for M15, but  $N_* \in [0.5, 0.7, 1.0, 1.4, 2.0] \times 10^6$ ,  $d \in [2.6, 3.7, 5.2, 7.6, 10.5] \text{ kpc}$ ,  $\eta \in [0.005, 0.055]$ ,  $\log_{10}(\dot{E}) \in [33.9, 34.9]$  in steps of 0.05, and  $N_{\text{MSP}} \in [5, 299]$  in steps of 1. We conducted a maximum of  $N_t = 10^7$  trials, with  $N_{\text{comb}} = 2.9 \times 10^6$  for M15 and  $N_{\text{comb}} = 7.4 \times 10^6$  for  $\omega \text{ Cen}$ , respectively (cf. Figure 5, where the value of  $N_t$  is indicated in each panel).

## 4 RESULTS

### 4.1 The H.E.S.S. GC Population

To obtain a sample of GCs suited for the study by H.E.S.S., Abramowski et al. (2013) selected a population of clusters based on the GC catalog of Harris (2010) from which all the basic parameters such as position,  $d$ ,  $r_c$ , and central luminosity density  $\rho_0$  have been taken. Abramowski et al. (2013) furthermore applied different cuts on the target and observation run lists:

1. GC  $|\text{Galactic latitude}| \geq 1.0^\circ$ . This cut was done to conservatively exclude GCs towards the direction of the Galactic Plane to avoid faint emission from unresolved sources, diffuse emission, and

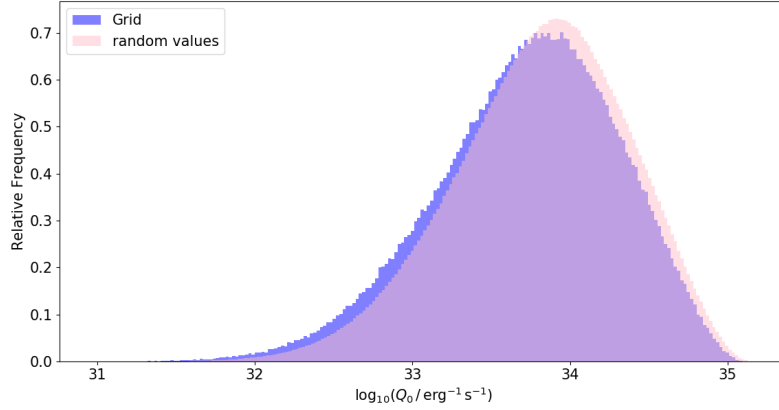


**Figure 3.** Histogram of  $\log_{10}(Q_0)$  obtained via two different methods: sampling from a grid or randomly sampling for a set range for four free parameters. The pink histogram has a median  $Q_{0,\mu} = 7.0 \times 10^{33} \text{ erg}^{-1} \text{ s}^{-1}$ , 16<sup>th</sup> percentile of  $1.8 \times 10^{33} \text{ erg}^{-1} \text{ s}^{-1}$ , and 84<sup>th</sup> percentile of  $2.3 \times 10^{34} \text{ erg}^{-1} \text{ s}^{-1}$  whilst the blue histogram has  $Q_{0,\mu} = 5.9 \times 10^{33} \text{ erg}^{-1} \text{ s}^{-1}$ , 16<sup>th</sup> percentile of  $1.4 \times 10^{33} \text{ erg}^{-1} \text{ s}^{-1}$ , and 84<sup>th</sup> percentile of  $2.0 \times 10^{34} \text{ erg}^{-1} \text{ s}^{-1}$

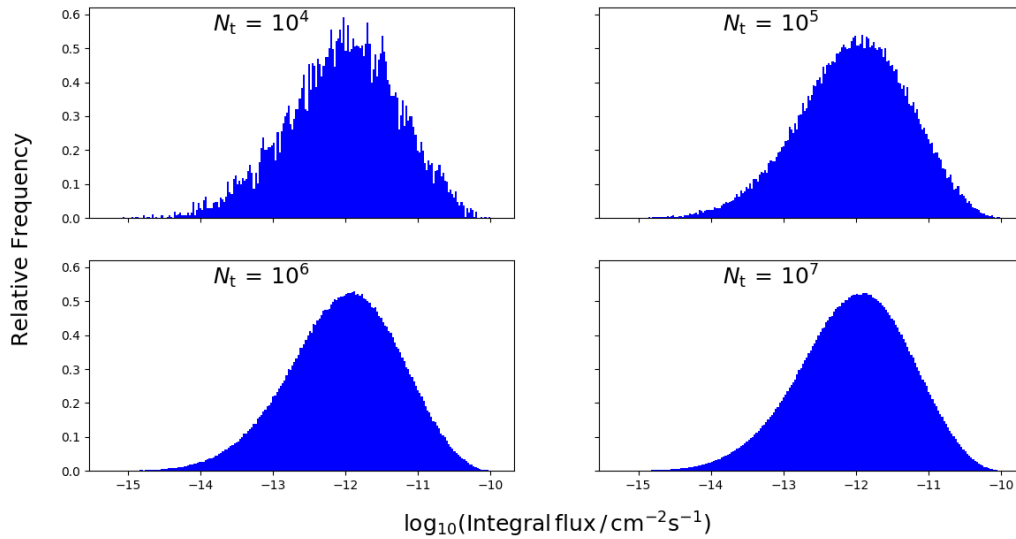


**Figure 4.** Histograms of  $\log_{10}(F(E > 0.72 \text{ TeV}) / \text{cm}^{-2} \text{ s}^{-1})$  for different  $N_t$  as indicated in each panel, for 47 Tucanae, and for 7 free parameters.

also chance coincidences with unrelated sources.

2. Standard quality selection criteria were applied, with the telescopes pointed  $< 2.0^\circ$  offset from the GC position.

3. A selected GC had to have at least 20 available runs passing the cut describe in point 2. to ensure a reasonably long exposure on these potentially faint sources.

In order to compare our model predictions with the H.E.S.S. flux upper limits  $F_{UL}$ , we have to characterise the mean predicted flux plus its uncertainty<sup>4</sup> First, we obtain the median flux  $F_\mu$  (50<sup>th</sup> percentile) for each cluster, as well as the 16<sup>th</sup> and 84<sup>th</sup> percentile, as

<sup>4</sup> We note that it is common in certain statistical contexts to use the 2<sup>nd</sup> quartile (median) as an indication of an average value, and the 1<sup>st</sup> and 3<sup>rd</sup> quartiles (25<sup>th</sup> and 75<sup>th</sup> percentiles) as indications of uncertainty or the spread of values around the median, as is done in box plots. However, we opt to use the median and the 16<sup>th</sup> and 84<sup>th</sup> percentiles to estimate the average

shown in Figure 6 and listed in Table 1. We calculate  $\sigma_{16} = \mu - F_{16}$  and  $\sigma_{84} = F_{84} - \mu$  and also express them as percentages:  $100\sigma_{16}/\mu$  and  $100\sigma_{84}/\mu$ , with  $F_{16}$  and  $F_{84}$  being the 16<sup>th</sup> and 84<sup>th</sup> percentiles. We also calculate the geometric mean of the flux  $\bar{F}_G$  (since we want to be insensitive to outliers), as well as the standard deviation  $\sigma$  of this flux, noting that the geometric mean is equal to the antilog of the arithmetic mean of the log of fluxes. We finally list the ratios  $F_\mu/F_{UL}$  as well as  $\bar{F}_G/F_\mu$ , indicating that the median is usually

and uncertainty in model flux (in analogy to what is typical for a normal distribution of values), as is commonly done in certain physics contexts, given the fact that our flux distributions appear to be approximately log-normal. Our main conclusion, that there are large uncertainties on the median model fluxes due to uncertainty on model parameters, is not affected by this choice of convention.



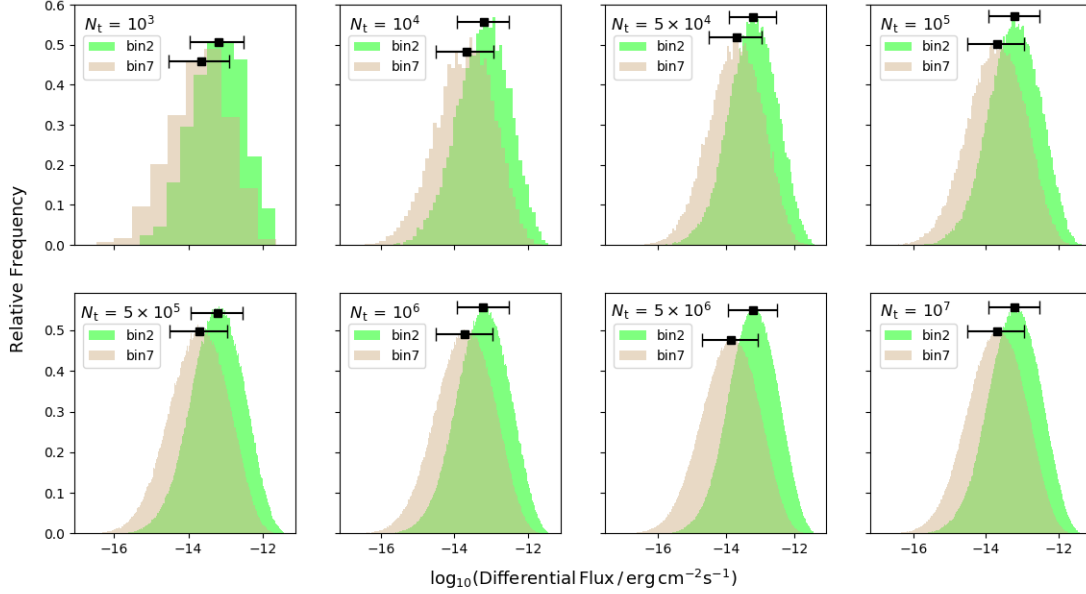


**Figure 5.** Distribution plots of  $\log_{10}$  of the differential flux for MAGIC bin 2 ( $E = 62$  GeV) and bin 7 ( $E = 954$  GeV), with the median and  $1\sigma$  uncertainties indicated by the black square and error bars. The  $x$ -axis shows the  $\log_{10}$  of the  $\nu F_\nu$  flux while the  $y$ -axis shows the normalised frequency. The number of trials  $N_t$  in each case is indicated in each panel.

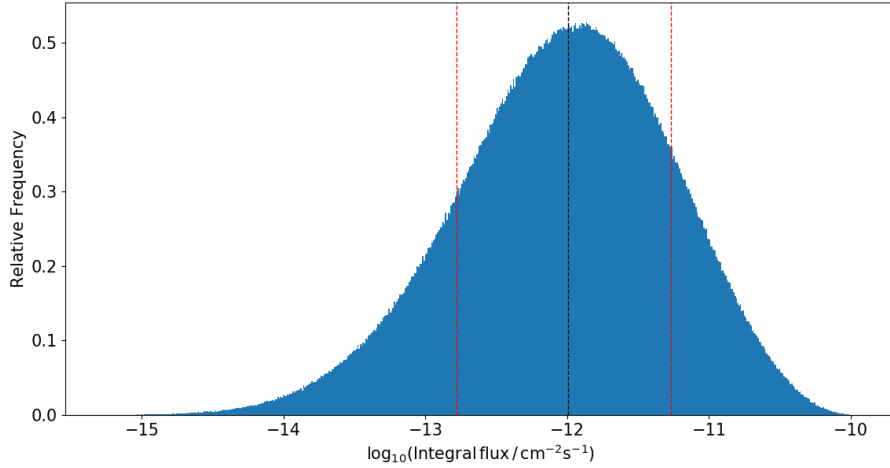


**Figure 6.** Histogram of  $\log_{10}(F(E > 0.72 \text{ TeV}) / \text{cm}^{-2}\text{s}^{-1})$ . The  $x$ -axis shows the  $\log_{10}$  of integral flux while the  $y$ -axis shows the normalised frequency. The red dashed lines represent the 16<sup>th</sup> and 84<sup>th</sup> percentiles, and black dashed line shows the median of the integral flux distribution for 47 Tucanae.

below the upper limit, except for Djorg 2 and the stacking upper limit, and that  $F_\mu \approx \bar{F}_G$ .

In Figure 7 we show the distribution of the  $\log_{10}$  of weighted (stacked) flux for all GCs. We plot the weighted flux as a function of  $N_t$  for all 15 GCs. We use  $E_{\text{th}} = 0.23$  TeV and calculate the weighted flux as

$$F_w = \sum_{i=1}^{15} \frac{\tau_i}{\tau_{\text{tot}}} \times F_i(> 0.23 \text{ TeV}), \quad (4)$$

where  $i$  represents a specific GC,  $\tau_i$  is the live time (acceptance-

corrected observational time passing quality cuts) for each GC, and  $\tau_{\text{tot}}$  is the total live time. The median and geometric mean of this quantity are listed in the bottom row of Table 1, in column 4 and 8, respectively, for comparison to the stacked upper limit published by H.E.S.S. as listed in column 3. The first set (range) of parameter combinations used for the green histograms in Figure 7 is as follows:  $d_{\text{cluster}} \in [\frac{d}{2}, \frac{d}{\sqrt{2}}, d, \sqrt{2}d, 2d]$ ,  $N_* \in [\frac{N}{2}, \frac{N_*}{\sqrt{2}}, N_*, \sqrt{2}N_*, 2N_*]$  (see Venter & Kopp 2015 for values of  $d$  and  $N_*$ ). We used  $B \in [1, 9]$  in steps of 2,  $\Gamma \in [1.7, 2.9]$  with steps of 0.3,  $\eta \in [0.005, 0.08]$  in steps of 0.0075,  $\log_{10}\langle E \rangle \in [33.7, 34.7]$  in steps of 0.1, and

**Table 1.** H.E.S.S. flux upper limits from Abramowski et al. (2013) as well as model predictions corresponding to a first set of parameter combinations (associated with the green histograms in Figure 7). The columns in the Table are: the GC name; energy threshold of the analysis, defined as the location of the peak in the distribution of reconstructed photon energies; integral photon flux upper limits (99% confidence level following Feldman & Cousins 1998) assuming a power law with an index of 2.5 (Abramowski et al. 2013)  $F_{\text{UL}}(E > E_{\text{th}})$ ; median of  $\log_{10}$  of integral flux distribution  $F_{\mu}$ ; ratio between the  $\sigma_{16}$  and the median; ratio between  $\sigma_{84}$  and the median; ratio between the median and the flux upper limit; geometric mean to characterise distributions with a significant variation across many orders of magnitude; ratio between standard deviation  $\sigma$  and the median; and the ratio between the geometric mean and median. The bottom row represents results for a stacking scenario, i.e.,  $F_{\text{UL}}(E > E_{\text{th}})$  represents the live-time-weighted flux of 15 GCs, while the modelling results (cf. Eq. 4) are for the same 15 GCs, and weighted similarly.

GC name	$E_{\text{th}}$ (TeV)	$F_{\text{UL}}(E > E_{\text{th}})$ $\times 10^{-13}$ ( $\text{ph cm}^{-2}\text{s}^{-1}$ )	$F_{\mu}$ $\times 10^{-13}$ ( $\text{ph cm}^{-2}\text{s}^{-1}$ )	$\sigma_{16}/F_{\mu}$ (%)	$\sigma_{84}/F_{\mu}$ (%)	$F_{\mu}/F_{\text{UL}}$	$\bar{F}_G$ $\times 10^{-13}$ ( $\text{ph cm}^{-2}\text{s}^{-1}$ )	$\sigma/F_{\mu}$ (%)	$\bar{F}_G/F_{\mu}$
NGC 104	0.72	19	10.0	84	427	0.53	9.4	611	0.92
NGC 6388	0.28	15	5.9	85	461	0.39	5.5	706	0.93
NGC 7078	0.40	7.2	1.7	84	465	0.24	1.5	673	0.94
Terzan 6	0.28	21	6.9	86	518	0.33	6.3	890	0.91
Terzan 10	0.23	29	11.0	87	530	0.38	10.0	903	0.91
NGC 6715	0.19	9.3	1.2	85	478	0.13	1.1	722	0.92
NGC 362	0.59	24	1.5	88	572	0.06	1.4	1081	0.93
Pal 6	0.23	12	11.0	87	534	0.92	9.9	919	0.90
NGC 6256	0.23	32	3.2	87	534	0.10	2.9	941	0.91
Djorg 2	0.28	8.4	10.0	86	508	1.19	9.2	831	0.92
NGC 6749	0.19	14	6.9	87	534	0.49	6.3	913	0.91
NGC 6144	0.23	14	4.3	87	554	0.31	3.9	972	0.91
NGC 288	0.16	5.3	6.1	87	553	1.15	5.6	945	0.92
HP 1	0.23	15	5.4	87	539	0.36	5.0	925	0.93
Terzan 9	0.33	45	2.8	89	644	0.06	2.6	1341	0.93
Stacking analysis	0.23	3.3	25	50	119	7.6	26.0	135	1.04

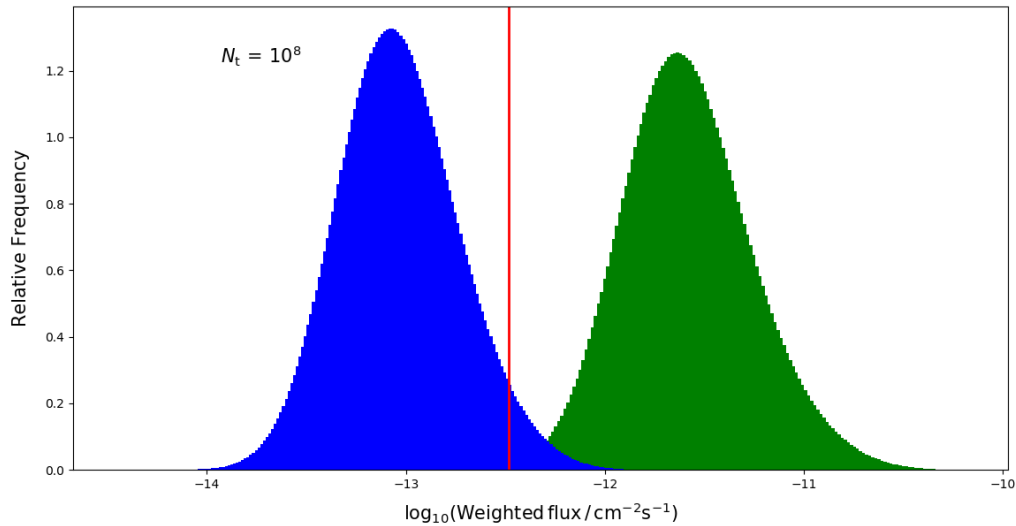


**Figure 7.** Distribution of  $\log_{10}(F_w(E > E_{\text{th}}) / \text{cm}^{-2}\text{s}^{-1})$  for all GCs. The x-axis shows the  $\log_{10}$  of total weighted flux while the y-axis shows the normalised frequency. The green histograms are associated with the first parameter combination, while the blue ones are for the second parameter combination. The red line represents the stacked upper limit as noted in Table 1. We used  $N_t = 10^8$ .

$N_{\text{MSP}} \in [5, 150]$  in steps of 10. Although somewhat arbitrary, these were chosen to be an example set of reasonable (best-guess) parameter values. However, we see from Table 1 that for this initial choice, the median stacked flux exceeds the upper limit by a factor of 7.6. We therefore considered a second parameter set, associated

with the blue histograms of weighted flux for 15 GCs in Figure 7:  $\eta \in [0.003, 0.03]$  in steps of 0.003,  $\log_{10}(\dot{E}) \in [33, 34]$  in steps of 0.1, and  $N_{\text{MSP}} \in [5, 50]$  in steps of 5. Again, this choice might seem arbitrary, but given the freedom in model parameters, there is no unique way of reducing the GC flux. Thus, we reduced the three

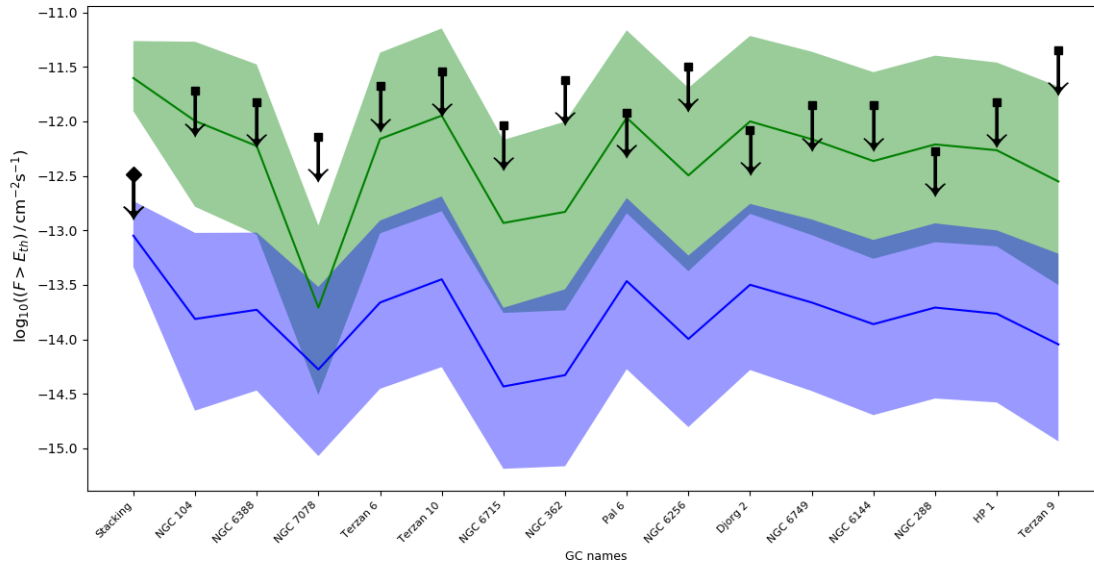


**Figure 8.** Flux upper limits (black diamond and squares with arrows) on the observed  $\gamma$ -ray flux from the population of GCs, as well as the predicted flux medians plus  $1\sigma$  uncertainties (green and blue) for each of the two parameter combinations. The first entry indicates the stacked (live-time-weighted) flux with  $1\sigma$  uncertainties, as indicated in Table 1.

**Table 2.** H.E.S.S. flux upper limits and model predictions for the second parameter combination, associated with the blue histograms in Figure 7.

GC name	$E_{\text{th}}$ (TeV)	$F_{\text{UL}}(E > E_{\text{th}})$ $\times 10^{-13}$ ( $\text{ph cm}^{-2}\text{s}^{-1}$ )	$F_{\mu}$ $\times 10^{-13}$ ( $\text{ph cm}^{-2}\text{s}^{-1}$ )	$\sigma_{16}/F_{\mu}$ (%)	$\sigma_{84}/F_{\mu}$ (%)	$F_{\mu}/F_{\text{UL}}$	$\bar{F}_G$ $\times 10^{-13}$ ( $\text{ph cm}^{-2}\text{s}^{-1}$ )	$\sigma/F_{\mu}$ (%)	$\bar{F}_G/F_{\mu}$
NGC 104	0.72	19	0.154	86	614	0.0081	0.145	929	0.94
NGC 6388	0.28	15	0.187	82	410	0.0125	0.179	610	0.96
NGC 7078	0.40	7.2	0.053	84	573	0.0074	0.051	737	0.95
Terzan 6	0.28	21	0.218	84	463	0.0104	0.208	766	0.92
Terzan 10	0.23	29	0.356	84	475	0.0123	0.337	778	0.95
NGC 6715	0.19	9.3	0.037	82	429	0.0040	0.035	622	0.96
NGC 362	0.59	24	0.047	85	513	0.0020	0.044	923	0.94
Pal 6	0.23	12	0.343	85	578	0.0286	0.324	787	0.94
NGC 6256	0.23	32	0.101	84	482	0.0032	0.096	810	0.95
Djorg 2	0.28	8.4	0.317	84	451	0.0377	0.302	713	0.95
NGC 6749	0.19	14	0.218	84	577	0.0156	0.205	780	0.94
NGC 6144	0.23	14	0.138	86	492	0.0097	0.129	819	0.93
NGC 288	0.16	5.3	0.196	85	492	0.0370	0.183	806	0.93
HP 1	0.23	15	0.172	85	481	0.0115	0.162	797	0.95
Terzan 9	0.33	45	0.090	87	580	0.0020	0.084	1147	0.93
Stacking analysis	0.23	3.3	0.895	48	108	0.271	0.923	113	1.03

(degenerate) main parameters determining the source strength  $Q_0$ , i.e.,  $\eta$ ,  $\dot{E}$ , and  $N_{\text{MSP}}$  by a factor of a  $\sim 3$  to illustrate that by lowering  $Q_0$ , the flux upper limits may be satisfied. While we do not claim this second set as a final answer, we deem these ranges to still be realistic, given the uncertainty in their intrinsic values. The fluxes obtained for the second choice of parameter grid are indicated in Table 2. In this case, the predicted median flux is a factor of  $\sim 4$  below the H.E.S.S. upper limit (indicated by the red solid line in Figure 7). This is one example (i.e., changing some parameters so as to yield a smaller  $Q_0$ ) of how one can use the H.E.S.S. data to constrain the MSP population's characteristics (see also [Ndiyavala et al. 2019](#)), although there may be some degeneracy with other

model parameters such as  $\kappa$ ,  $\Gamma$ ,  $d$  and to a lesser extent  $B$  (this will impact the SR component more) and  $N_*$ , although the latter is relatively well constrained.

Finally, we graphically summarise the fluxes we obtained for both the stacked as well as single-GC cases in Figure 8. The black diamond and squares and arrows correspond to the observational upper limits, while the green and blue squares and error bars are for the median fluxes and  $1\sigma$  uncertainty intervals, for the two different parameter combinations as discussed above. We note that there are indeed parameter combinations that yield fluxes below all of these observational upper limits. One example is afforded by combinations of degenerate parameters yielding a lower  $Q_0$ ; there may also



be other parameter combinations that can lower the flux, as indicated before. Further constraints derived from future observations may aid in breaking such degeneracies.

## 4.2 M15

The northern GC M15 (also known as NGC 7078) is one of the densest<sup>5</sup> globular clusters ever discovered in the Milky Way Galaxy. It has undergone a core collapse contraction and thus belongs to the class of core-collapsed brightest GCs (Acciari et al. 2019). M15 hosts at least eight MSPs detected so far (Freire 2015). It is located at a distance of  $d = 10.4$  kpc (Harris 1996) at RA (J2000)  $21^{\text{h}}29^{\text{m}}58^{\text{s}}.33$  and Dec  $+12^{\circ}10'01''.2$  (Galactic coordinates:  $l = 65.01^{\circ}$ ,  $b = -27.31^{\circ}$ ) and exhibits  $r_c = 0'.14$  and a half-light radius  $r_h = 1'.00$  (Harris 1996).

Acciari et al. (2019) observed M15 with the MAGIC telescopes, since it is the only GC discovered by *Fermi* LAT at GeV  $\gamma$ -ray energies that they could observe at low zenith angles. Its  $\gamma$ -ray luminosity measured above 0.1 GeV is  $L_{\gamma}^{\text{M15}} = (5.26_{-1.16}^{+1.31}) \times 10^{34} \text{ erg s}^{-1}$  and the spectrum is similar to the power-law type with spectral index  $2.84 \pm 0.18$  when observed up to  $\sim 5$  GeV (Zhang et al. 2016). The estimated number of MSPs in M15 is  $37_{-8}^{+9}$ , for a conversion efficiency of the MSP's spin-down power into GeV  $\gamma$ -rays of  $\eta_{\gamma} \approx 0.08$  and an average luminosity of  $\langle L_{\gamma}^{\text{MSP}} \rangle = 1.44 \times 10^{33} \text{ erg s}^{-1}$  per MSP. However, no detection from the direction of M15 has been made in the TeV band (Acciari et al. 2019). These authors therefore followed Rolke et al. (2005) using a 95% confidence level and assuming a 30% total systematic uncertainty on the collection area and spectral index of  $-2.6$  to calculate the upper limits on the VHE flux from the source. They found an upper limit of  $F(E > 0.3 \text{ TeV}) = 3.2 \times 10^{-13} \text{ cm}^{-2} \text{ s}^{-1}$ , which several times more stringent than the  $F(E > 0.44 \text{ TeV}) = 7.2 \times 10^{-13} \text{ cm}^{-2} \text{ s}^{-1}$  published earlier by Abramowski et al. (2013).

We create a distribution of differential fluxes (see Figure 5 for energy bins 2 and 7, centred on energies of  $E = 62$  GeV and  $E = 955$  GeV, respectively) and calculate the median and  $1\sigma$  uncertainties of the  $\log_{10}$  of these fluxes by finding the 16<sup>th</sup>, 50<sup>th</sup> and 84<sup>th</sup> percentiles. As before, the fluxes were obtained by randomising over seven free parameters many times (see the different  $N_i$  as indicated in each panel) to study the convergence.

Figure 9 shows the upper limits from 165 hrs of MAGIC observations on the differential flux, the predicted spectrum for a few different combinations of model parameters, and the median points with  $1\sigma$  error. We note that the differential data are much more constraining than the integral data since there are 13 points of comparison instead of 1. For each bin, we are able to tell whether the model exceeds the flux at that energy bin or not, thus constraining the spectral shape. For our choice of parameters, we satisfy the MAGIC flux upper limits.

## 4.3 $\omega$ Cen

$\omega$  Centauri (NGC 5139), which is located at RA  $201.7^{\circ}$ , Dec  $-47.56^{\circ}$ , stands out among all the known GCs in our Galaxy. Its origin and history are not fully understood yet, but its properties have led to suggestions that it may be the remnant core of a dwarf galaxy that has been disrupted (e.g., Bekki & Freeman 2003).  $\omega$  Cen is the most massive, complex, brightest, and has the largest core and half-light radius of all GCs in the Galaxy (Harris 1996).

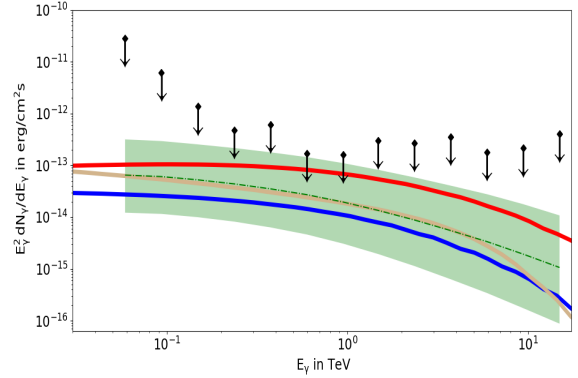


**Figure 9.** Differential flux upper limits (black diamonds with arrows) on the  $\gamma$ -ray flux from M15 plus a few typical model spectra (solid lines) for typical parameter combinations, as well as predicted medians and  $1\sigma$  error bars (green error band). For the example fits, we used lepton energies of  $E_{\text{min}} = 0.01 \text{ TeV}$ ,  $E_{\text{max}} = 100 \text{ TeV}$ , assumed Bohm diffusion,  $B = 5\mu\text{G}$ ,  $\Gamma = 1.9$ , and  $Q_0 = 1.81 \times 10^{33} \text{ erg}^{-1} \text{ s}^{-1}$  (red line);  $E_{\text{min}} = 0.01 \text{ TeV}$ ,  $E_{\text{max}} = 30 \text{ TeV}$ ,  $k_0 = 7 \times 10^{-5} \text{ kpc}^2/\text{Myr}$ ,  $B = 3\mu\text{G}$ ,  $\Gamma = 2.1$ , and  $Q_0 = 4.75 \times 10^{32} \text{ erg}^{-1} \text{ s}^{-1}$  (blue line) and  $E_{\text{min}} = 0.01 \text{ TeV}$ ,  $E_{\text{max}} = 30 \text{ TeV}$ ,  $k_0 = 1.0 \times 10^{-3} \text{ kpc}^2/\text{Myr}$ ,  $B = 5\mu\text{G}$ ,  $\Gamma = 1.9$ , and  $Q_0 = 1.81 \times 10^{33} \text{ erg}^{-1} \text{ s}^{-1}$  (golden line).

It is thought to have been the nuclear star cluster of either the Sequoia or Gaia-Enceladus Galaxy discussed in Myeong et al. (2019). The cluster also shows characteristic features such as its incredible multiplicity in stellar populations (e.g., Pancino et al. 2000; Bellini et al. 2017) and its broad metallicity distribution (e.g., Freeman & Rodgers 1975; Magurno et al. 2019).  $\omega$  Cen is furthermore suspected to harbour a black hole with total mass  $\sim 10^5 M_{\odot}$  at its centre, which makes this GC an interesting candidate to model for possible future CTA observations (Zocchi et al. 2019).

Observations by *Fermi* LAT has indicated that  $\omega$  Cen's spectrum was reminiscent of a typical MSP spectrum. However, it was a mystery that no radio or X-ray MSPs had been detected (Abdo et al. 2010) at that time. The Parkes Radio Telescope has now detected five radio MSPs in this cluster, four of which are isolated and a fifth one is in an eclipsing binary system. This confirms the scenario that the cumulative MSP  $\gamma$ -ray emission may explain the *Fermi* detection of this cluster. However, no pulsations in the GeV data have been found to date (Dai et al. 2020).

We apply the same method as in Section 3.2 on  $\omega$  Cen as an example of a Southern source. In Figure 10 we compare the predicted differential fluxes with the H.E.S.S. and CTA sensitivity curves for 100 hours of observations. We also indicate typical predicted  $\gamma$ -ray spectra for a few choices of parameter combinations. We note that our current IC predictions are higher than predicted by Ndiyavala et al. (2018). This is because Ndiyavala et al. (2018) assumed relatively low numbers of stars within this cluster, while we now use  $N_* = 10^7$  (Miller & Walker 2020), creating a much higher ambient target photon density.

## 5 DISCUSSION AND CONCLUSIONS

A number of models attempt to explain the multi-wavelength spectra detected from several Galactic GCs. In addition to the broad leptonic and hadronic scenarios described in Section 1, there are

<sup>5</sup> <https://www.nasa.gov/feature/goddard/2017/messier-15>

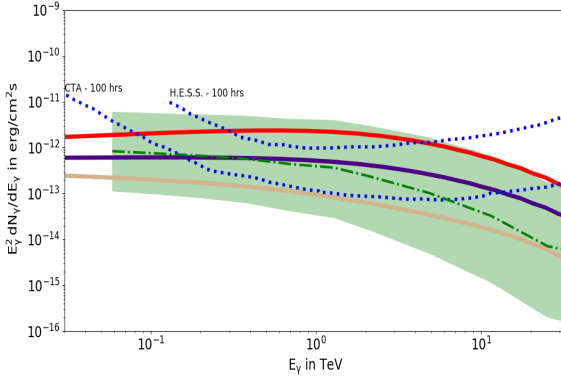


**Figure 10.** Differential flux predictions (green error band) for  $\omega$  Cen, the solid lines indicating example predictions. The blue dashed lines represent the H.E.S.S. and CTA sensitivity curves for 100 hours of observations (Funk et al. 2013). For the example spectra, we chose  $E_{\min} = 0.001$  TeV and  $E_{\max} = 100$  TeV for all cases. We then assume Bohm diffusion,  $B = 5\mu G$ ,  $\Gamma = 1.9$ , and  $Q_0 = 8.17 \times 10^{33} \text{ erg}^{-1} \text{ s}^{-1}$  (red line);  $\kappa_0 = 7 \times 10^{-5} \text{ kpc}^2/\text{Myr}$ ,  $B = 3\mu G$ ,  $\Gamma = 2.1$ , and  $Q_0 = 2.40 \times 10^{33} \text{ erg}^{-1} \text{ s}^{-1}$  (violet line) and  $k_0 = 1.0 \times 10^{-3} \text{ kpc}^2/\text{Myr}$ ,  $B = 1\mu G$ ,  $\Gamma = 2.3$ , and  $Q_0 = 7.57 \times 10^{32} \text{ erg}^{-1} \text{ s}^{-1}$  (golden line).

other processes or refinements that we did not consider in this paper, but that can significantly influence the level of the predicted TeV emission from GCs. For example, Bednarek & Sobczak (2014) performed numerical calculations of the asymmetric TeV  $\gamma$ -ray emission morphology produced by the interaction of stellar winds leaving the GC and the Galactic medium, which should create a bow shock nebula around GC. Furthermore, Bednarek et al. (2016) considered the role of advection of leptons within the GC by the mixture of winds from the embedded populations of MSPs and other stellar members, as well as the effect of a non-central location of a dominating, energetic MSP, on the predicted  $\gamma$ -ray flux. In order to constrain or discard some of these models, careful testing of them is needed.

This paper focused on assessing uncertainties in the predicted VHE  $\gamma$ -ray flux of GCs within the context of the leptonic GC model of Kopp et al. (2013), with the main aim to give theoretical guidance to CTA’s observational strategy. We demonstrated that uncertainty in model parameters leads to a large spread in the predicted flux. We modelled the IC  $\gamma$ -ray flux expected from 15 GCs that have been observed, but not detected, by H.E.S.S. in the VHE band. We confirmed that a finer grid in parameter space leads to a smoother flux distribution, as expected. Furthermore, a larger number of trials led to convergence of the flux distribution, as  $N_t \rightarrow N_{\text{comb}}$ . Also, the eventual predicted range of fluxes depends on the number of free model parameters, as well as their respective ranges.

Interestingly, we could demonstrate the power of using a stacking approach: the relative errors on the predicted live-time-weighted flux is nearly one order of magnitude lower than that for the individual GCs. This well-known effect is also apparent in the observational upper limits, where the weighted-flux upper limit is lower and therefore more constraining than the single-GC ones (Figure 8). We also note that the median flux and geometric mean flux were very close. The different methods of estimating the error on the mean flux yielded slightly different, yet broadly consistent results, but one can appreciate the large spread (uncertainty) in predicted fluxes based on these error estimates.

We found that while none of our predicted individual cluster median fluxes plus uncertainties violated the respective upper limits (Figure 8), our total integral weighted flux violated the H.E.S.S. upper limit for our first set of parameter combinations (Table 1). However, one has to be careful to summarily discard models if calculations for best-guess parameters exceed observational limits, noting the considerable uncertainty in predictions that may stem from uncertain parameter values. Our second parameter combination satisfied the stacked upper limits (Table 2). Thus we could use this stringent upper limit to constrain the source properties of the MSPs embedded within the GC. For M15, we found that the differential upper limits were more constraining than the H.E.S.S. integral flux upper limits. Yet, we could satisfy these upper limits for typical parameters. As an example of a Southern-hemisphere source, we calculated the TeV flux for  $\omega$  Cen, indicating that this source may be a possible candidate to be observed by H.E.S.S. or CTA.

In conclusion, we note that increasing measurement accuracy on model parameters will improve predictions of GC fluxes, and this will provide better guidance to CTA’s observations. Future refined models will have to undergo continued scrutiny, also taking into account the effect of parameter uncertainty on their predictions, as they are confronted with new data.

## 6 ACKNOWLEDGMENTS

The Virtual Institute for Scientific Computing and Artificial Intelligence (VI-SCAI) is gratefully acknowledged for operating the High Performance Computing (HPC) cluster at the University of Namibia (UNAM). VI-SCAI is partly funded through a UNAM internal research grant. We also acknowledge discussions with James Allison and Leonard Santana. This study was financially supported by the African German Network of Excellence in Science (AGNES), through the “Programme Advocating Women in Science, Technology, Engineering and Mathematics”. This work is based on the research supported wholly / in part by the National Research Foundation of South Africa (NRF; Grant Numbers 87613, 90822, 92860, 93278, and 99072). The Grantholder acknowledges that opinions, findings and conclusions or recommendations expressed in any publication generated by the NRF supported research is that of the author(s), and that the NRF accepts no liability whatsoever in this regard.

## 7 DATA AVAILABILITY

Data available on request - The data underlying this article will be shared on reasonable request to the corresponding author.

## References

- Abdo A. A., et al., 2009, *Science*, 325, 848
- Abdo A. A., et al., 2010, *A&A*, 524, A75
- Abramowski A., et al., 2011, *A&A*, 531, L18
- Abramowski A., et al., 2013, *A&A*, 551, A26
- Acciari V. A., et al., 2019, *MNRAS*, 484, 2876
- Aharonian F., et al., 2009, *A&A*, 499, 273
- Anderhub H., et al., 2009, *A&A*, 498, 83
- Bednarek W., 2012, *J. of Phys.*, 39, 065001
- Bednarek W., Sitarek J., 2007, *MNRAS*, 377, 920
- Bednarek W., Sobczak T., 2014, *MNRAS*, 445, 2842
- Bednarek W., Sitarek J., Sobczak T., 2016, *MNRAS*, 458, 1083

- Bekki K., Freeman K. C., 2003, *MNRAS*, **346**, L11
- Bellini A., Milone A. P., Anderson J., Marino A. F., Piotto G., van der Marel R. P., Bedin L. R., King I. R., 2017, *ApJ*, **844**, 164
- Brown A. M., Lacroix T., Lloyd S., BÅ'hm C., Chadwick P., 2018, *Phys.~Rev.~D.*, **98**, 041301
- Cheng K. S., Chernyshov D. O., Dogiel V. A., Hui C. Y., Kong A. K. H., 2010, *ApJ*, **723**, 1219
- Clapson A.-C., Domainko W., Jamrozy M., Dyrda M., Eger P., 2011, *A&A*, **532**, A47
- Dai S., Johnston S., Kerr M., Camilo F. o., Cameron A., Toomey L., Kumamoto H., 2020, *ApJ*, **888**, L18
- Domainko W. F., 2011, *A&A*, **533**, L5
- Eger P., Domainko W., Clapson A.-C., 2010, *A&A*, **513**, A66
- Feldman G. J., Cousins R. D., 1998, *Phys. rev. D*, **57**, 3873
- Freeman K. C., Rodgers A. W., 1975, *ApJ*, **201**, L71
- Freire P., 2015, Pulsars in globular clusters, <http://www.naic.edu/~pfreire/GCpsr.html>
- Funk S., Hinton J. A., CTA Consortium 2013, *Astropart.~Phys.*, **43**, 348
- Harding A. K., Usov V. V., Muslimov A. G., 2005, *ApJ*, **622**, 531
- Harris W. E., 1996, *AJ*, **112**, 1487
- Harris W. E., 2010, arXiv:1012.3224,
- Kong A. K. H., Hui C. Y., Cheng K. S., 2010, *ApJ*, **712**, L36
- Kopp A., Venter C., Büsching I., de Jager O. C., 2013, *ApJ*, **779**, 126
- Lang K. R., 1993, *Astrophysical Data: Planets and Stars*, Heidelberg: Springer-Verlag
- Magurno D., et al., 2019, *ApJ*, **881**, 104
- Manchester R. N., Johnston S., 1995, *ApJ*, **441**, L65
- McCutcheon M., 2009, arXiv e-prints, p. arXiv:0907.4974
- Miller M., Walker J., 2019 (accessed July 26, 2020), Millions of Stars in Omega Centauri. [https://www.nasa.gov/mission\\_pages/hubble/multimedia/ero/ero\\_omega\\_centauri.html](https://www.nasa.gov/mission_pages/hubble/multimedia/ero/ero_omega_centauri.html)
- Myeong G. C., Vasiliev E., Iorio G., Evans N. W., Belokurov V., 2019, *MNRAS*, **488**, 1235
- Ndiyavala H., Krüger P. P., Venter C., 2018, *MNRAS*, **473**, 897
- Ndiyavala H., Venter C., Johnson T. J., Harding A. K., Smith D. A., Eger P., Kopp A., van der Walt D. J., 2019, *The Astrophysical Journal*, **880**, 53
- Pancino E., Ferraro F. R., Bellazzini M., Piotto G., Zoccali M., 2000, *ApJ*, **534**, L83
- Rolke W. A., López A. M., Conrad J., 2005, *Nuclear Instruments and Methods in Physics Research A*, **551**, 493
- Tam P. H. T., Kong A. K. H., Hui C. Y., Cheng K. S., Li C., Lu T.-N., 2011, *ApJ*, **729**, 90
- Venter C., Kopp A., 2015, Proc. SAIP2014, ed. C Engelbrecht and S Karataglidis, ISBN: 978-0-620-65391-6, pp 394–9
- Venter C., de Jager O. C., 2005, *ApJ*, **619**, L167
- Venter C., de Jager O. C., 2008, *ApJ*, **680**, L125
- Venter C., de Jager O. C., 2010, *ApJ*, **725**, 1903
- Venter C., de Jager O. C., Clapson A.-C., 2009, *ApJ*, **696**, L52
- Zajczyk A., Bednarek W., Rudak B., 2013, *MNRAS*, **432**, 3462
- Zhang P. F., Xin Y. L., Fu L., Zhou J. N., Yan J. Z., Liu Q. Z., Zhang L., 2016, *MNRAS*,
- Zocchi A., Gieles M., Hénault-Brunet V., 2019, *MNRAS*, **482**, 4713

This paper has been typeset from a  $\text{\TeX}/\text{\LaTeX}$  file prepared by the author.